An Investigation of the Relationship between Emission and Scattering Signals in SSM/I Data

GUOSHENG LIU AND JUDITH A. CURRY

Program in Atmospheric and Oceanic Sciences, Department of Aerospace Engineering Sciences, University of Colorado, Boulder, Colorado

(Manuscript received 5 December 1995, in final form 17 October 1996)

ABSTRACT

To provide guidance for the development of satellite microwave rainfall-retrieval algorithms, the basic relationships between emission and scattering signals in natural clouds must be understood. In this study, the relationship between two parameters observed from microwave satellite data—the polarization difference at 19 GHz D and the polarization-corrected temperature PCT—is investigated over the global ocean on a monthly and 5° (lat) × 5° (long) mean basis. Using data from January and July 1993, the occurrence frequencies and latitudinal variation and horizontal distribution of the D–PCT relationships are investigated. The D–PCT slope is studied by dividing the entire weather range into three regimes: nonprecipitation, light precipitation, and heavy precipitation. The analysis shows that small variation of PCT in the nonprecipitation regime could be achieved by employing a variable coefficient in the PCT definition equation. The slopes in the light precipitation regime are latitude dependent. Although the interpretation is inconclusive, it is felt that the differences in the fractional coverage and the rain layer depth in different latitudes is responsible for the latitudinal dependence. No clear latitudinal dependence of slopes in the heavy precipitation regime is found.

The connection of the D–PCT relationship to the performances of an emission-based and a scattering-based rainfall algorithm are investigated using the Second WetNet Precipitation Intercomparison Project rainfall cases. The results of this study emphasize the necessity of incorporating the scattering signal in rainfall rate retrieval algorithms. Additionally, the D–PCT slope information can be used to help categorize precipitation types, which may be useful in determining the specific algorithm best used for a certain precipitation type and/or regime.

1. Introduction

Microwave signals measured from a satelliteborne radiometer can be generally classified into two categories based on how the microwave field interacts with the atmospheric hydrometeors: emission and scattering. At low frequencies where the scattering of upwelling radiation by ice particles is negligible, the satellite-received radiance over a radiatively cold ocean varies in correspondence to the change in the total amount of liquid hydrometeors in the atmosphere. A higher liquid water amount translates to a higher brightness temperature. This is the so-called ''emission signal.'' On the other hand, scattering by large ice particles at high frequencies reduces the amount of radiation reaching the satellite. A higher concentration of ice particles aloft results in a lower brightness temperature. This is usually called the ''scattering signal.''

A number of studies have used the scattering or the emission signal or a combination of both to investigate atmospheric hydrometeors. Retrievals of liquid water path in an atmospheric column are based on the emission signal from lower microwave frequencies, such as 19.35 and 37 GHz (e.g., Greenwald et al. 1993; Liu and Curry 1993; Petty 1990), while evaluation of precipitating ice has been made using the scattering signal at 85.5 GHz (Spencer et al. 1989; Grody 1991; Liu et al. 1994). Rainfall retrieval algorithms have been designed using either or both the emission and the scattering regimes because both the amounts of liquid water below the freezing level and ice water above are statistical measures of rainfall rate on the ground. Early work by Wilheit et al. (1977, 1991) presented a rainfall algorithm that is purely emission based, using the 19.35-GHz frequency. Adler et al. (1993) and Ferraro and Marks (1995) developed scattering-based rainfall algorithms that use the depression of the 85.5-GHz brightness temperature by ice scattering as the key variable. Coupling of the emission and the scattering signals was attempted by Liu and Curry (1992) and Petty (1994a, b) in order to overcome problems such as saturation of the emission signal at lower frequency and high rain rates, and the low sensitivity of the scattering signal to low rain rates. In recent years several additional coupled algorithms have been developed. Wilheit et al. (1994) provided a

Corresponding author address: Dr. Guosheng Liu, Program in Atmospheric and Oceanic Sciences, Department of Aerospace Engineering Sciences, University of Colorado, Boulder, CO 80309-0429. E-mail: liug@colorado.edu

detailed review of the algorithms submitted to the First WetNet Precipitation Intercomparison Project (PIP-1). In addition, Liu et al. (1995) used a coupled microwave emission and scattering parameter to represent the overall intensity of the microwave signal from cloud and precipitation and studied the cloud and precipitation characteristics in the equatorial western Pacific warm pool. Devlin and Zipser (1995) investigated the mesoscale convective systems in the tropical and subtropical regions based on 85.5-GHz polarization-corrected temperature (PCT) defined by Spencer et al. (1989). Modeling and observational studies of the emission and scattering signals for individual cloud systems have been done by Smith et al. (1992) and Heymsfield and Fulton (1994), among many others.

Although the microwave emission and scattering signals are widely used in meteorological studies, their relationships in actual cloud systems have yet to be addressed in a climalotological context over the entire globe. The main purpose of this study is to examine the relationship between emission and scattering signals in most oceanic areas over the globe. We also investigate how the emission–scattering relationship affects emission- and scattering-based algorithms using selected Second WetNet Precipitation Intercomparison Project (PIP-2) cases. By investigating the emission–scattering relationship, this study aims both to understand some of the characteristics of natural cloud systems and to improve current rainfall-retrieval algorithms.

2. Definition of the SSM/I emission and scattering signals

The Special Sensor Microwave/Imager (SSM/I) has seven separate total-power radiometers at frequencies of 19.35, 22.235, 37, and 85.5 GHz (hereafter referred to as 19, 22, 37, and 85 GHz). Dual-polarization measurements are taken at 19, 37, and 85 GHz, while only vertical polarization is observed at 22 GHz. The spatial resolution ranges from 69 × 43 km at 19 GHz to 15 × 13 km at 85 GHz. Brightness temperatures of nine 85-GHz pixels are averaged to match that of one 19-GHz pixel in order to obtain similar spatial coverage for the two channels. The SSM/I swath width is 1394 km on the earth's surface and the antenna beam intersects the normal to the earth's surface at an angle of 53°. Sampling for the *F11* satellite occurs in early morning and late afternoon. Because of orbital drift the sampling time for the *F10* satellite occurs roughly around midday and midnight. The local sampling frequency is about twice a day using data from both satellites.

At lower microwave frequencies, the brightness temperature is more directly related to the emission of liquid hydrometeors, so that a larger amount of liquid water in an atmosphere column produces a stronger emission signal. One indicator of the emission signal is the brightness temperature itself at a low frequency. However, the brightness temperature is also a function of the physical temperature of the emitter. Therefore, to analyze the emission signal, we use the polarization difference of brightness temperature (D) at 19 GHz:

$$D = T_{BV19} - T_{BH19}, \tag{1}$$

where T_{BV19} and T_{BH19} are, respectively, the vertically and horizontally polarized brightness temperatures at 19 GHz. Because strong emission in the atmosphere reduces the polarization difference of the radiation from the highly polarized ocean surface, the polarization difference is representative of the atmospheric emission itself. The advantage of using D over brightness temperature is that the strongest emission signature yields a value of D close to 0, independently of the physical atmospheric temperature.

To represent the scattering signature we use the PCT for 85 GHz (Spencer et al. 1989), which is expressed by

$$\mathrm{PCT} = (1 + \alpha)T_{BV85} - \alpha T_{BH85}, \tag{2}$$

where T_{BV85} and T_{BH85} are, respectively, the vertically and horizontally polarized brightness temperatures at 85 GHz. Spencer et al. (1989) determined a value of $\alpha = 0.818$, which was originally designed to keep values of PCT almost constant when there is no precipitation and/or ice clouds. However, a single value of α cannot achieve this goal because of the high sensitivity of PCT to background radiation from sea surface and clear-sky variables (Petty 1994a,b). As will be shown in the following sections, latitudinal and seasonal variations of PCT in nonprecipitating conditions are very significant when a fixed value of α is used. When the atmosphere is optically thick and $T_{BV85} \approx T_{BH85}$, PCT no longer depends on α but mainly reflects the brightness temperature depression due to the scattering by ''dense ice'' particles, such as graupel, hail, and freezing raindrops. Therefore, PCT is a good indicator of scattering in this weather range. Although PCT in (2) does not solely represent the scattering signal, we use it in this study because, unlike 85-GHz brightness temperature, PCT is monotonic when the water vapor, cloud water, and rainfall increase.

The variables D and PCT were used by Liu et al. (1995) in their microwave index that combines both emission and scattering signals. Petty (1994a,b) defined another set of emission and scattering indicators in which the influences from the oceanic state and atmospheric gases are minimized. However, Petty's emission and scattering parameters require calculations of clear-sky brightness temperatures that cannot be derived directly from SSM/I data for raining pixels unless they are interpolated from nearby nonprecipitating pixels. The definitions of the emission and scattering signals in this study are very similar to Petty's, only in the present study these parameters are not normalized by clear-sky radiation.

Although both D and PCT decrease with increasing rainfall rate, the relative changes of the two parameters are related to the structure of the precipitating cloud.

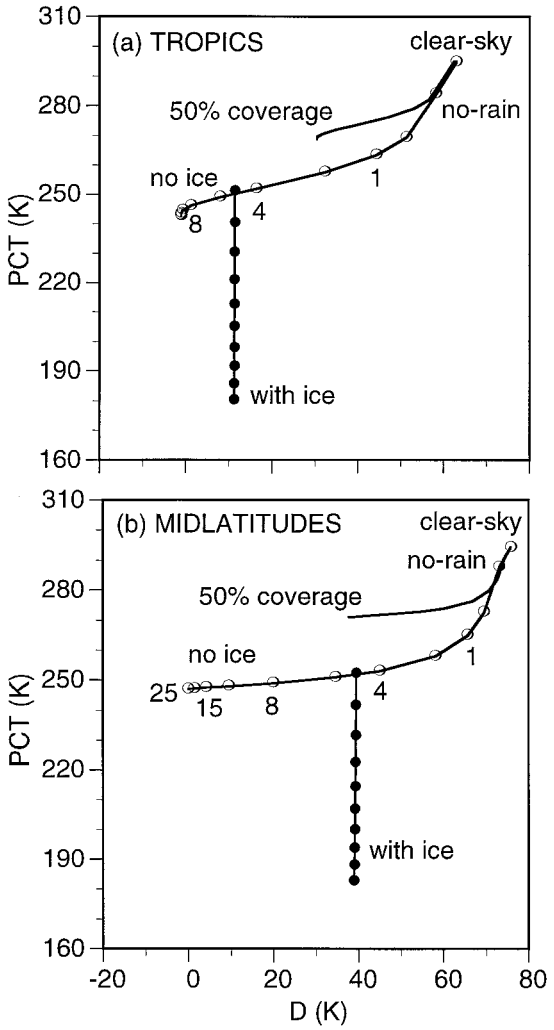

FIG. 1. The relationship between D and PCT as simulated by a radiative transfer model. The numbers (1, 4, 8, 15, and 25) indicate rainfall rate in mm h^{-1}. See text for more detailed explanation.

Figure 1 shows the results from a plane-parallel radiative transfer model (Liu and Curry 1992, 1993) of modeled values of D and PCT for several idealized clouds. To solve the radiative transfer equation, the atmosphere was divided vertically into 15 1-km layers. All geophysical variables are assumed to be constant in each layer. The equation is then solved by an iterative method. Ice particles are treated as spheres because of the complexity in habit and orientation of natural ice particles in clouds. However, the model results are intended to show qualitatively that the presence of ice reduces the amount of high-frequency radiation, but not the exact amount reduced. Therefore, it is thought that this approximation is adequate for this purpose.

The tropical case (Fig. 1a) is based on the *U.S. Standard Atmosphere* tropical atmospheric temperature and water vapor profiles with freezing level at 5 km. A cloud with liquid water path of 400 g m^{-2} is assumed to be located just below the freezing level. Two different rain types are assumed: one (marked ''no ice'') is a rain layer below freezing level in which the rainfall rates are the same in all altitudes. The depth of the rain layer does not change when the rainfall rate increases from 0 (marked ''no-rain'') to 25 mm h^{-1}. The circles on the left of no-rain denote rainfall rates of 0.5, 1, 2, 4, 6, 8, 10, 15, 20, and 25 mm h^{-1}. Also, the point corresponding to ''clear sky'' is shown in the figure. The other rain type (marked ''with ice'') has the same rainfall-rate profile as rainfall rate of 5 mm h^{-1} in the no ice case below freezing level, but a 5-km ice layer is added above freezing level. The ice particles are assumed to be spherical with density of 0.5 g cm^{-3}. Ice water path varies from 0 to 2000 g m^{-2}, corresponding to downward change of the solid dots. A curve marked ''50% coverage'' denotes that only 50% of the pixel is covered by no ice rain and the other 50% is clear sky. In Fig. 1b the U.S. standard midlatitude atmosphere is used in which the freezing level is at 2 km and the depth of the rain layer is changed accordingly to 2 km.

For the no ice cases, D decreases with increasing rainfall rate before it saturates near $D = 0$. For tropical conditions D saturates for rainfall rates of about 10 mm h^{-1} because we have assumed a deep rain layer (5 km). In midlatitudes, the saturation of D occurs at 15 mm h^{-1}. The largest decreases in PCT result from an increase in cloud and rain amount when the rainfall rate is very light (<1 mm h^{-1}) and an increase in ice water amount above freezing level. Changes in fractional coverage of rain and rainfall rate also cause changes in PCT, although these effects are relatively small. All these processes need to be taken into account when interpreting observed D–PCT relationships for light rainfall because both partial rain coverage of a pixel and ice particles aloft reduce PCT. However, if a pixel is completely covered by rain with rainfall rates exceeding 1 mm h^{-1}, the PCT values are more closely related to the amount of ice above the freezing level. Also, it is noted that the magnitudes of D for clear sky are larger in midlatitudes than in the Tropics because of the higher water vapor amount in the tropical atmosphere.

3. Results

SSM/I data from both *F10* and *F11* in January and July of 1993 are used in this study. Because the emission signal of condensed atmospheric water is distinguishable from the underlying surface only over open water, we will limit our studies to oceanic area between 60°S and 60°N. Examination of both January and July illustrates the seasonal difference of the emission and scattering signals.

a. Monthly averaged relationship between D and PCT

To obtain monthly mean relationships between D and PCT, we average observations of PCT in every 1 K bin

of D for every 5° (lat) × 5° (long) area. Figure 2 shows the D–PCT relationship in several selected regions. The rain threshold determined by Liu and Curry (1992) is also shown on each diagram by an upward arrow; data points having values of D (or PCT) larger than that at the arrow are determined to be nonprecipitating. It is interesting that for the cases shown here the rain threshold seems to divide the points into two parts with different slopes. We examined the D–PCT relationship in all the 5° × 5° boxes between 60°S and 60°N during the 2 months and found that this is also true for most of the data, especially for the regions where low values of D (<20 K) and PCT (<240 K) are observed. In the subtropical case (Fig. 2f), PCT values change by only a few degrees while values of D change by more than 30 K. Few deep clouds could have occurred in this region. However, PCT variations in nonprecipitating conditions are larger for most of the other regions, especially for high-latitude cases.

By examining the monthly averaged D–PCT relationship in all the 5° × 5° boxes, we have categorized them into 5 types based upon the pattern of the relationship.

Type 0: The ranges of both D and PCT are small. The minimum value of D is within 15 K of the rain threshold. Figure 2f is an example of Type 0.

Type 1: The minimum value of D is larger than 20 K, and D and PCT are related almost linearly in the precipitation portion. Figure 2k is an example of Type 1.

Type 2: The minimum value of D is larger than 20 K. Apparent downward curvature is observed in the D–PCT scatterplot. Figure 2j is an example of Type 2.

Type 3: The minimum value of D is less than 20 K. The D–PCT scatterplot in the precipitation portion is approximately linear. Examples include Figs. 2c, 2e, 2g, 2h, and 2l.

Type 4: The minimum value of D is less than 20 K. Apparent downward curvature is observed in the D–PCT scatterplot. Examples include Figs. 2a, 2b, 2d, and 2i.

For some cases, the discrimination between Type 3 and Type 4 is not obvious. However, as will be shown later, the slope in the $D < 20$ portion of D–PCT plot is significantly different for Type 3 cases from for Type 4 cases. Type 0 represents the regions where there are few rain events and virtually no heavy rainfall. Types 1 and 2 indicate the presence of some rainfall events but few heavy ones, while heavy rain events are expected in Type 3 and 4 regions. We compared the values of D with the threshold for deep convection as defined by Liu et al. (1995; microwave index $f = 0.75$, indicated in Fig. 2b by a downward-pointing arrow) and found that the deep convection threshold corresponds approximately to $D = 20$ K in the Tropics. Although $D = 20$ K could correspond to different precipitation intensities for different climatological regions, we will use it in this study as a boundary to divide heavy from moderate rainfall. Devlin and Zipser (1995) used PCT = 250 K to define mesoscale convective systems. It is noticed that PCT = 250 K is in correspondence to $D = 20$ K for most of the Type 3 and 4 cases shown in Fig. 2.

The D–PCT relationships shown in Fig. 2 are based upon monthly averages over 5° × 5° regions. The D–PCT relationship for an individual rain event could be different from the averaged pattern. In Fig. 2 the standard deviation of PCT in every D bin is shown by vertical lines. The deviation is very small in the nonprecipitation portion (usually $\sigma < 5$ K), while σ can be as large as about 20 K in the low D portion. However, despite the deviations, the overall trend of the D–PCT relationships is still similar to those of the averaged ones. Therefore, the averaged pattern used in this study is a meaningful representative of the D–PCT relationship.

Figure 3 shows the frequency of occurrence of each type for all 5° × 5° boxes between 60°S and 60°N in January and July 1993. The frequency distributions are quite similar between the two months: Types 1 and 3 are the most common types with about 40% and 30% frequency, respectively, and Type 2 is the rarest (<5%). Interestingly, in most regions (about 70%) D and PCT are approximately linearly related (Types 1 and 3) in the precipitation portion. This linear relation implies that, on the scales considered here, both the emission and the scattering signals are more likely to increase as precipitation increases, regardless of the intensity of the precipitation. As will be shown later, the rate of increase depends on latitude and/or climatological region.

The horizontal distribution and the zonally averaged frequency distribution of D–PCT types are shown in Figs. 4 and 5 for January and July. Type 0 is found in regions where shallow clouds are expected to be predominant, such as subtropics and eastern Pacific. Type 1 is dominant in the high latitudes (>40°) of both hemispheres. Type 2 is more frequently observed in the summer hemisphere. Types 3 and 4, which contain the major precipitation events, are more frequent in the Tropics and the summer hemisphere, particularly in the intertropical convergence zone (ITCZ) and South Pacific convergence zone (SPCZ) regions. Type 4 regions are usually embedded in Type 3 regions. The latitudinal frequency distribution in Fig. 5 shows maxima of total frequency of Type 3 and 4 in the midlatitude cyclone zones and near the equator. There are large January–July variations of total Type 3 and 4 populations in several regions, such as the southwestern Indian Ocean and northwestern Pacific, while a consistently high frequency of Types 3 and 4 is persistently observed in the ITCZ, SPCZ, and the Gulf Stream regions in the North Atlantic. More comparisons of Type 3 and 4 in different regions will be given in section 4.

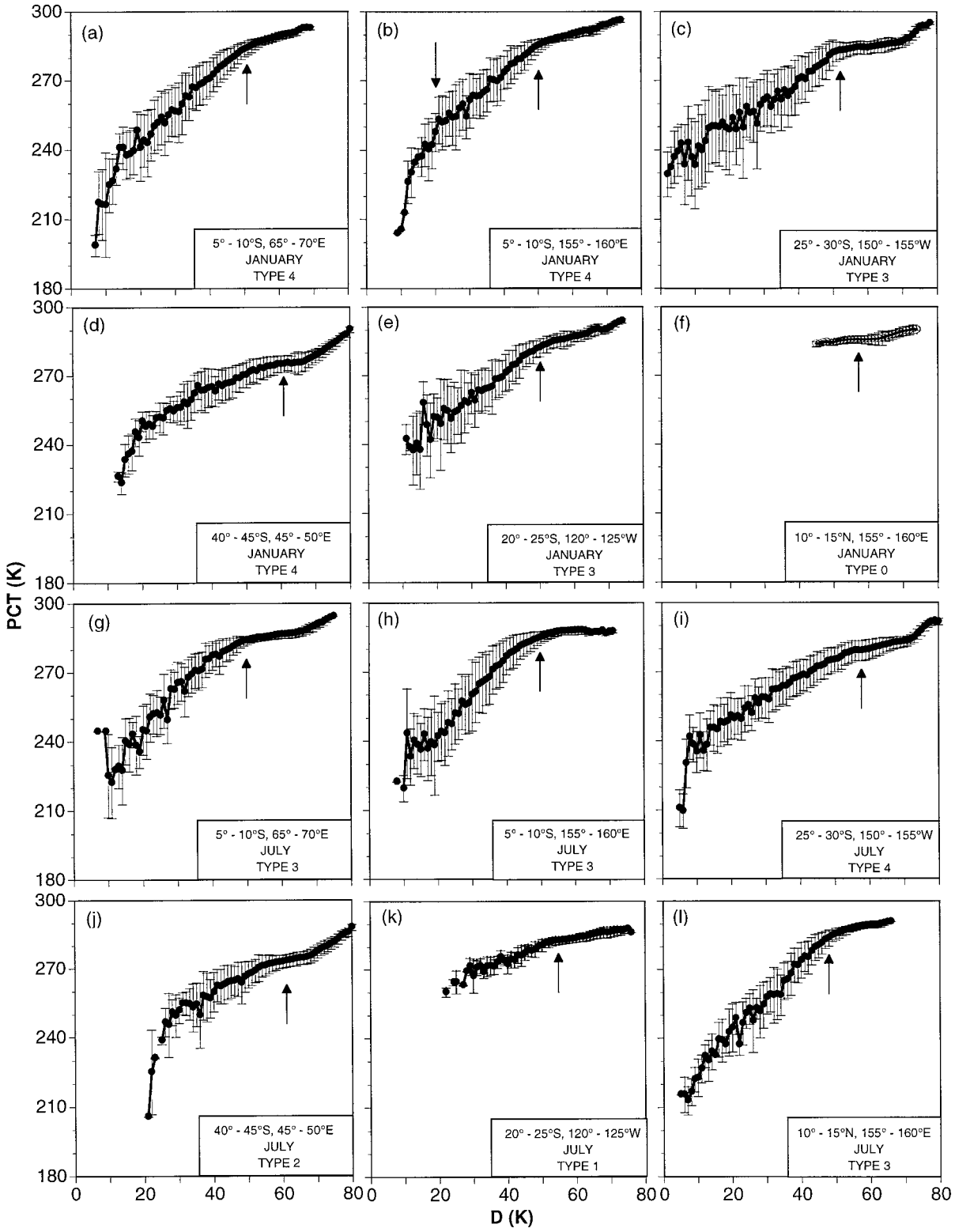

FIG. 2. Examples of monthly and 5° × 5° averaged relationship between *D* and PCT in SSM/I data. Up-pointing arrows indicate the rain threshold. The down-pointing arrow in (b) indicates the threshold for ''deep convection'' as defined by Liu et al. (1995). The type assigned to each relationship is also given. Standard deviation of PCT in each *D* bin is shown by vertical lines.

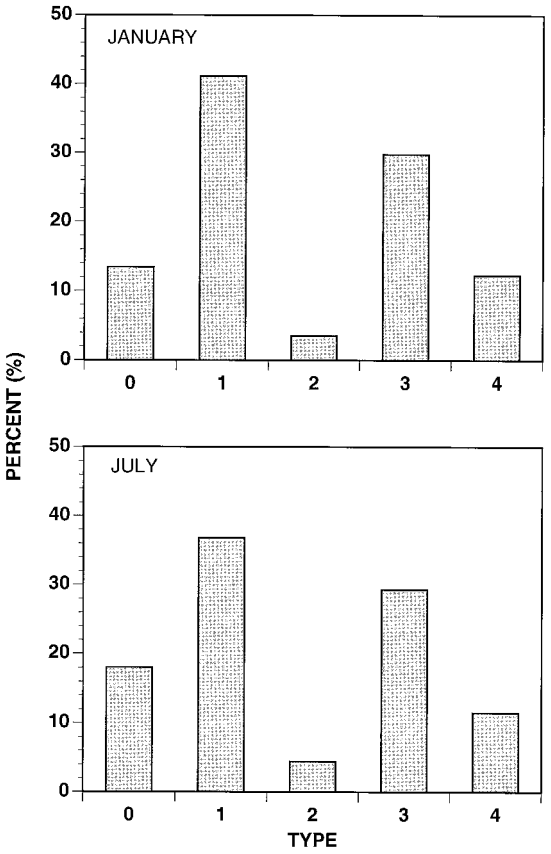

FIG. 3. Frequency distribution of each *D*–PCT type defined in this study.

b. Relationships between D and PCT *in different precipitation regimes*

In this section we examine further the *D*–PCT relationship at different precipitation intensity ranges. For this purpose, we divide the entire range into the following regimes.

1) Nonprecipitation regime: *D* and PCT are larger than those at the rain threshold. Changes in *D* and PCT are caused by the variation of sea surface state, water vapor amount, and cloud liquid water amount.
2) Light precipitation regime, which ranges from rain onset to $D = 20$ K: *D* varies almost linearly in this regime with PCT except for type 2, which comprises less than 5% of the $5^\circ \times 5^\circ$ boxes. The slope of the *D*–PCT scatterplot line reflects the different microphysical cloud structures and/or fractional coverage of the footprint by rain.
3) Heavy precipitation regime, which is comprised from the $D < 20$ K portion of Type 3 and 4.

We note here that the definition of the light and heavy precipitation regimes are not compatible with the National Weather Service definition of light and heavy rains, which are defined by rain rates.

Figure 6 shows the zonally averaged distribution of the percentages of pixel numbers assigned to each regime by the above definition. The percentages of the first and the second regime could vary depending on the ''tightness'' of the rain threshold. Larger (smaller) percentages will be assigned to the first regime if a threshold is tighter (looser). The threshold used in this study is tested by using midlatitude data (Liu and Curry 1992) and tropical data (Liu et al. 1995). This needs to be studied further, given that the data used for testing were very limited. One should keep this limitation in mind when interpreting the results in the figure. However, the general pattern of these distributions should remain valid regardless of some changes in the ''tightness'' of rain threshold. The nonprecipitation regime contributes about 90% of the total pixels in the 30°S–30°N belt. A larger percentage shows in the precipitation regimes in higher latitudes and it exhibits higher seasonal variability. Larger precipitation frequencies than those shown here might be the case in high latitudes, especially during the winter season because the SSM/I channels rarely detect snow precipitation. Petty (1995) studied the precipitation frequency over the global ocean using shipboard present-weather reports. In latitudes lower than 30°, this precipitation frequency is higher by several percent than that of this study if the precipitation events ''either near or at the ship at the time of the observation or during the preceding hour'' are all counted, but is lower by similar percentage if only the events ''occurring locally and at the actual time of the observation'' are counted. Because of the large footprint of the satellite pixels, we anticipate that the satellite precipitation frequency should be larger than that of a ship observed locally and at the actual time. Therefore, the frequency derived in this study for the lower latitude belt seems to be in a reasonable range. The frequency in higher latitudes (for example, higher than 40°) in the winter season is significantly lower in this study than Petty's. It is thought that this difference is mainly caused by the inability to detect falling snow by the SSM/I rain threshold, while Petty's precipitation frequency includes snow precipitation. The heavy precipitation regime ($D < 20$) has a very small overall percentage (<1%). In the following subsections, we investigate some of the characteristics in the *D*–PCT relationship for each of the three regimes.

1) NONPRECIPITATION REGIME

The nonprecipitation regime contains more than 70% of the observed SSM/I pixels (Fig. 6). As shown in the modeled (Fig. 1) and observed (Fig. 2) results, PCT usually does not remain a constant although there is no ice scattering. This PCT change results from the variation of sea surface and atmospheric states. To quantitatively describe this change, we calculated the slope in the $5^\circ \times 5^\circ$ averaged *D*–PCT scatterplot of the nonprecipitation regime assuming a linear approximation. A smaller slope means less change in PCT relative to

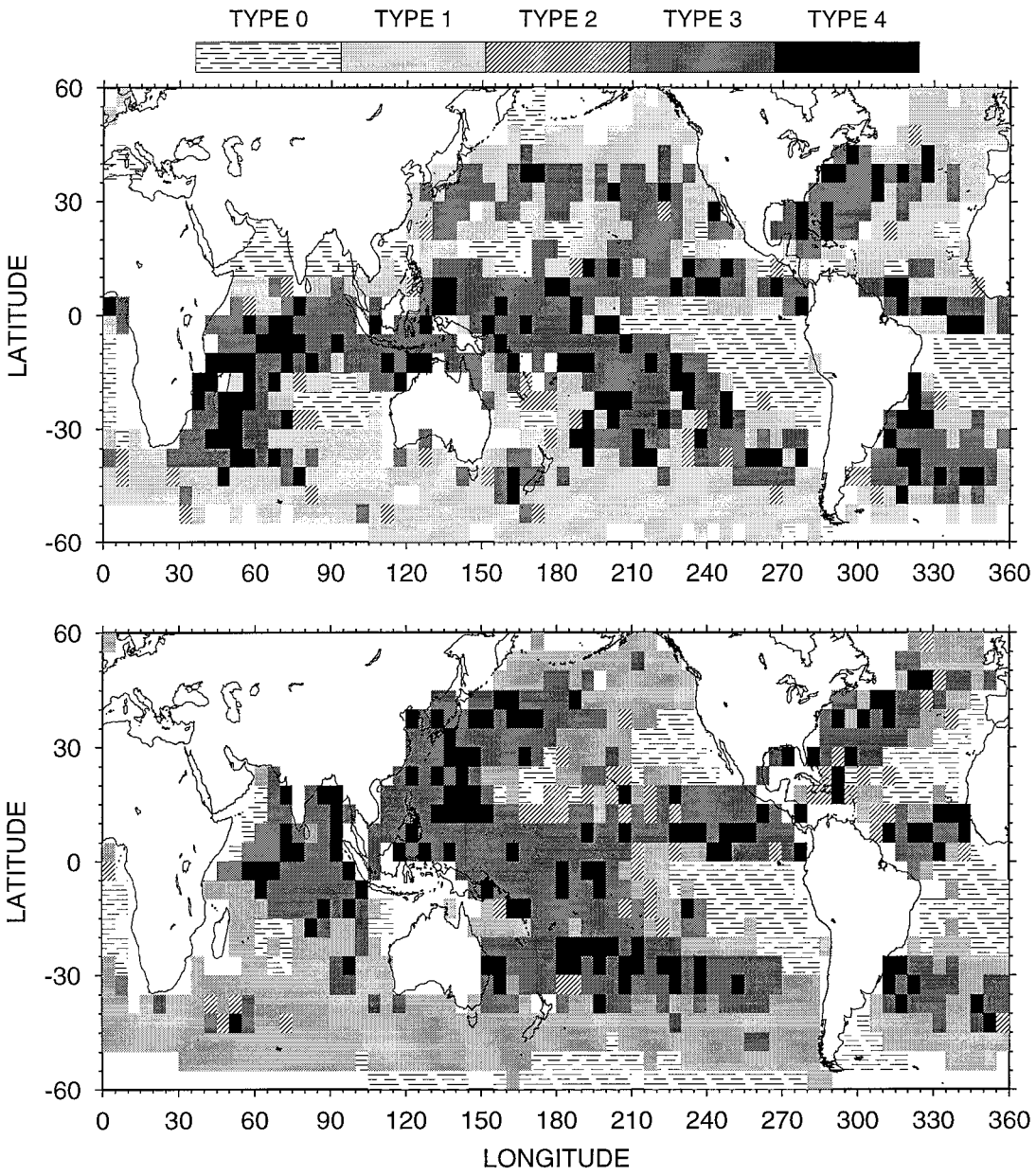

FIG. 4. Horizontal distribution of the *D*–PCT relationship types for January (top) and July (bottom) of 1993.

the change in *D*. The result is shown in Fig. 7. Basically, the slope varies with latitude and season, larger slopes occurring in higher latitudes and colder regions. The smallest slopes occur in the subtropical regions in the winter hemisphere. Between 30°S and 30°N the magnitude of the slope is less than 0.5. Therefore, the definition of PCT in (2) has its best performance in these low latitudes for minimizing the effects of nonscattering signals on the PCT.

2) LIGHT PRECIPITATION REGIME

Most of the raining pixels fall into this regime (Fig. 6). Similar to Fig. 7, the slopes in this regime are shown in Fig. 8. Type 2 data were excluded when calculating the slope because of their nonlinearity. Some of the Type 0 boxes were also excluded when the number of points met the rain threshold is less than 10, too few to calculate slope meaningfully. It is seen that slopes in this regime are also latitude and season dependent. However, contrary to those in the nonprecipitation regime, the largest slopes occur in the low latitudes and warmer regions. The different dependence of slope on latitude and season suggests that the dominant factor determining the *D*–PCT relationship differs in the light precipitation regime from that in the nonprecipitation regime.

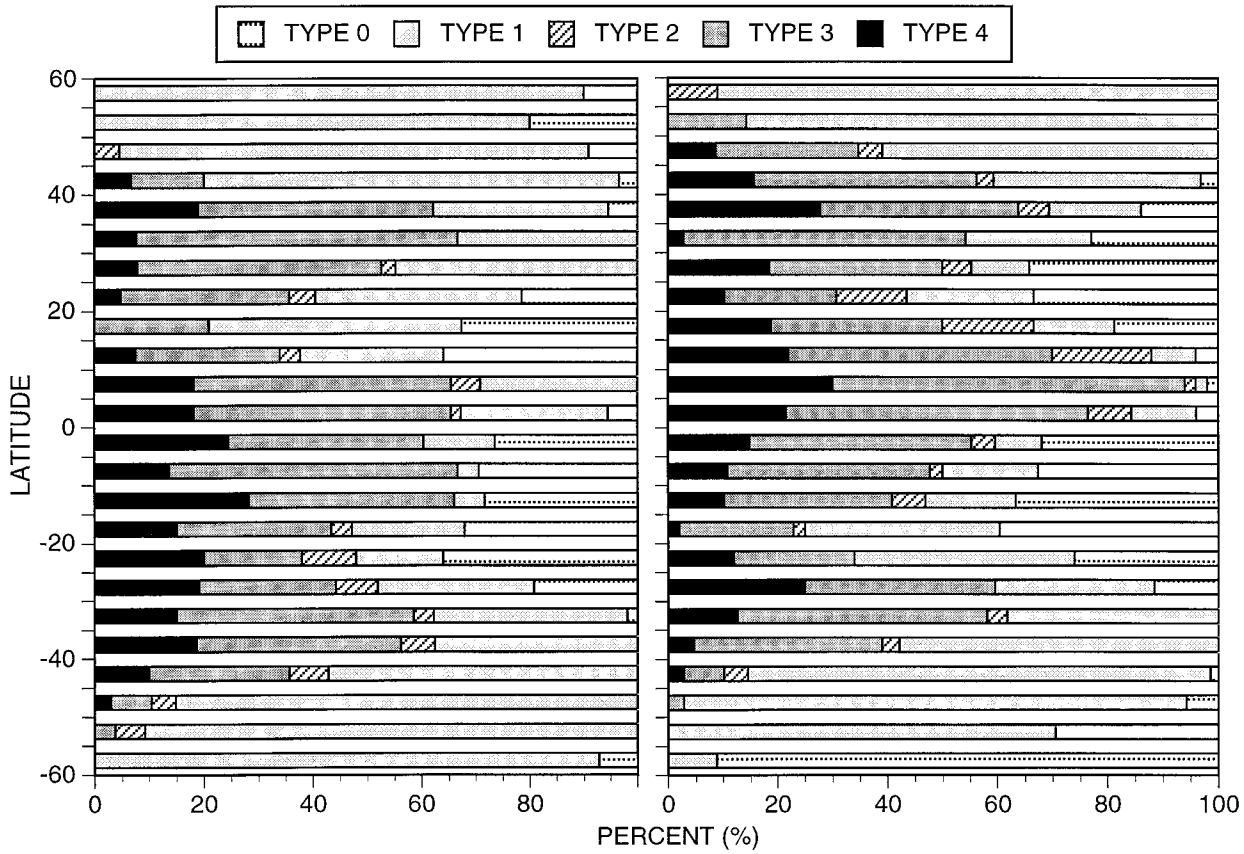

FIG. 5. Latitudinal distribution of the frequency of each type for January (left) and July (right) of 1993.

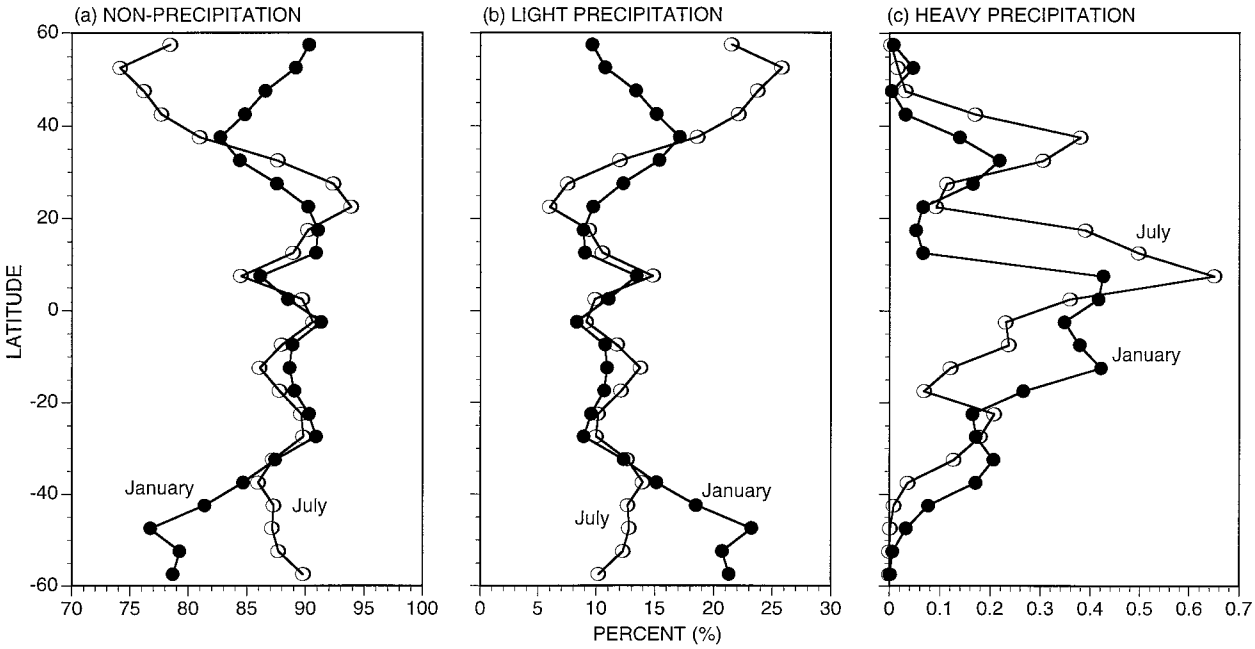

FIG. 6. Latitudinal distribution of the percentage of (a) nonprecipitation pixels, (b) light precipitation pixels, and (c) heavy precipitation pixels.

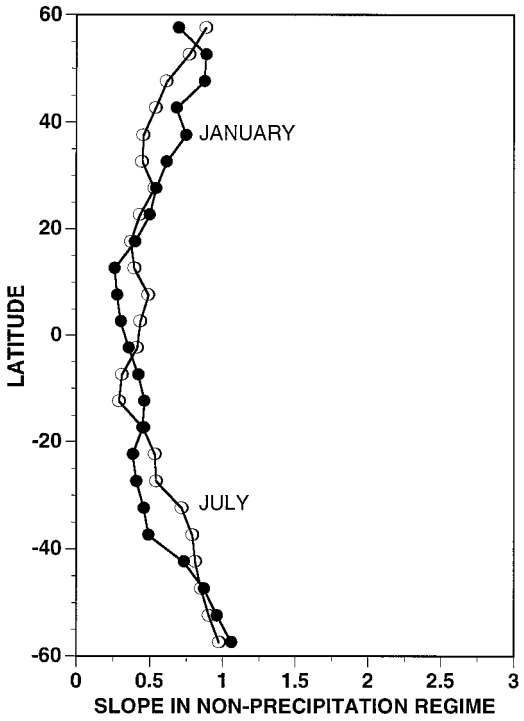

FIG. 7. Latitudinal distribution of slope in nonprecipitation regime for January and July of 1993.

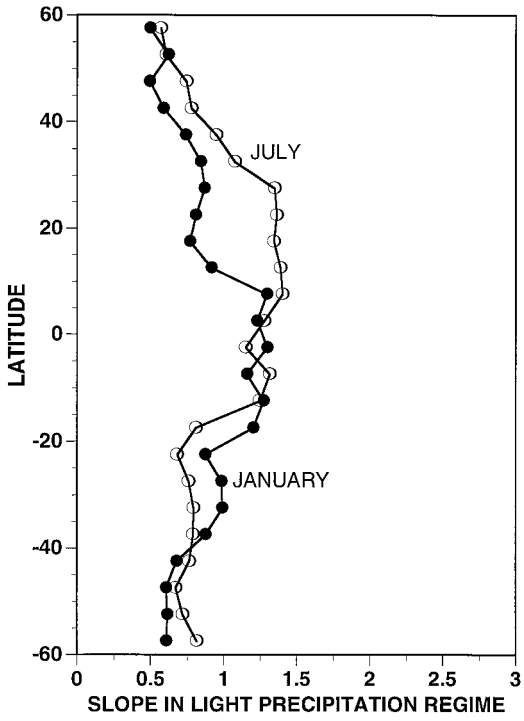

FIG. 8. Same as Fig. 7 except for light precipitation regime.

3) HEAVY PRECIPITATION REGIME

This regime only includes Type 3 and 4 boxes and amounts to fewer than 1% of the total pixels (Fig. 6). A slightly different way is used to calculate the slope in this regime because Type 4 usually has significant curvature. First, we find the intersection (point A) of $D = 20$ and the fitting line for the light precipitation regime. Next, we find the point (point B) in the heavy precipitation regime with maximum microwave index f (Liu et al. 1995), which is located in the left bottommost corner in the D–PCT scatterplot. The slope is then calculated for the line connecting points A and B. The results are shown in Fig. 9. Slight latitude dependence of the slope can be seen at latitudes higher than 30°. However, this dependence is very weak compared to the other two regimes. Instead, the slopes are dependent upon the types (3 or 4). The averaged slope of 641 Type 3 boxes is 1.1 and that of 257 Type 4 boxes is 3.7.

4. Interpretation and implication for rainfall retrievals

In the nonprecipitation regime, the D–PCT relationship is affected by the sea surface state and water vapor and cloud liquid water contents. For a given change in D, the change in PCT is larger in regions with colder sea surface temperature and lower water vapor and cloud liquid water amounts. This tendency is shown in both radiative transfer model results (Fig. 1) and observations

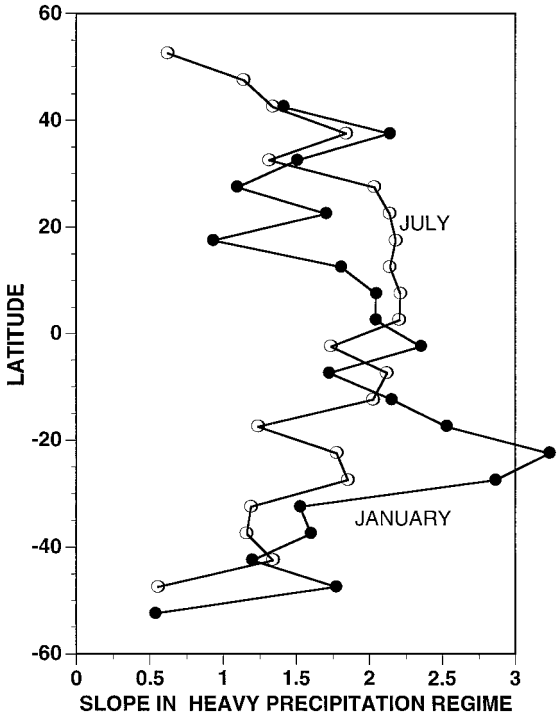

FIG. 9. Same as Fig. 7 except for heavy precipitation regime.

(Fig. 7). The *D*–PCT slope in the nonprecipitation regime can be varied by changing the value of α in (2). Figure 10 shows the *D*–PCT relationships for the same regions as in Fig. 2, but the value of α is adjusted for each region so that the slope in the nonprecipitation regime is minimized. When using PCT in a rainfall retrieval, it is hoped that PCT changes the least in the nonprecipitating regimes while PCTs in the precipitating regimes are sensitive to the change in rainfall rate. Adjusting α as in Fig. 10 is one way to achieve this goal. The zonally averaged values of adjusted α for the two months are shown in Fig. 11. The error bars show the standard deviations of α, which denote the zonal variation of α. The dashed curve is the best-fit curve to the average of α in both months, and can be expressed by

$$\alpha = 0.521 + 3.71 \times 10^{-4}x - 7.0 \times 10^{-5}x^2, \quad (3)$$

where x is latitude in degree with negative values for south and positive for north. Using α of this expression would decrease the variation of PCT in the nonprecipitation regime. The PCT with adjusted α is also useful when one attempts to use a coupled emission and scattering parameter, such as the microwave index f, used by Liu et al. (1995), because it minimizes the contributions of ''nonscattering'' variables (sea surface state, water vapor, and cloud liquid water) to the ''scattering signal'' (PCT). However, it is not optimal to utilize PCT as a rain threshold even with adjusted α because of the small difference between PCT values of no rain and light rain in some situations (e.g., see Figs. 10d,f,j).

In the light precipitation regime, the opposite latitudinal variation in *D*–PCT slope relative to the nonprecipitation regime suggests that the dominant factor(s) determining the *D*–PCT slope in this regime must be the rain layer itself, rather than sea surface and other atmospheric variables. The fact that changing α in (2) merely changes PCT in this regime also supports this interpretation. Three factors are anticipated to play the primary role in determining the slope: the amount of dense ice aloft, fractional rain coverage of a pixel, and the depth of rain layer. More dense ice above the freezing level leads to a sharper decrease in PCT, while no significant change occurs to *D* (refer Fig. 1), resulting in large values of the *D*–PCT slope. Fractional rain coverage of a pixel can change both *D* and PCT. Its effect on the *D*–PCT slope is complicated in that the pixel-averaged brightness temperature also depends on the horizontal geometry of the rain. In Fig. 1, the 50% rain coverage curve is also shown, which is obtained by calculating the pixel-averaged brightness temperature as simple spatial averages of clear-sky value and the plane-parallel model rain value. It is seen that the fractional coverage only slightly decreases the *D*–PCT slope in the precipitation regime. The simple averaging of clear-sky and plane-parallel model results could distort the real fractional coverage effect, as warned by Petty (1994a). So, the fractional coverage effect shown in Fig. 1 should be interpreted with caution. The effect of the depth of rain layer on the slope arises from the vertical temperature distribution of the rain layer. As rain rate increases, the peak of the weighting function moves to a higher altitude and consequently lowers the brightness temperature received by the satellite.

The radiative transfer model results in Fig. 1 show a larger slope for the 5-km rain layer in the Tropics than that for 2-km rain layer in the midlatitudes, except for very light rain conditions when the slope is partially affected by nonprecipitating factors. Because of the complexity of causes, the explanation for the latitudinal dependence of the *D*–PCT slope is not so obvious. More dense ice particles in the tropical clouds than in the higher-latitude clouds for this precipitation regime could be an explanation. However, as we will show later, the amount of dense ice is not necessarily greater in the low-latitude warm region than in higher latitudes. Another explanation could be that the tropical clouds are more convective, having larger horizontal and vertical dimensions as rainfall increases. Therefore, according to the discussions given above, the *D*–PCT slope should increase with rainfall rate because the depth and the fractional coverage of rain increase. If the increase is gradual and the total change is small, the *D*–PCT relationship is still approximately linear. But the slope is larger than those for the more stratiform clouds, in which depth and fractional coverage of rain exhibit no obvious change with the increase of rain rates. This idea is further supported by the fact that the large slopes are found in the tropical and subtropical convective zones, while in the midlatitude cyclone zones the values of the slopes are much smaller (Fig. 8). If this is the case, the slope value could help the developer of rainfall algorithms by accounting for the fractional coverage and rain-layer depth, although many difficulties remain unanswered in using this information. For example, this slope value could be used to distinguish the clouds in a region that is more convective than stratiform. Then a proper retrieval method could be applied according to this information.

The heavy precipitation regime, as mentioned in the previous section, corresponds to the deep convection cloud category described by Liu et al. (1995) in the tropical Pacific warm pool region. The depression of PCT is expected to be caused primarily by the presence of dense ice above the freezing level, because cloud systems falling within this regime are wide and deep so that the effects of fractional coverage and rain layer depth become unimportant. In other words, *D* and PCT are almost orthogonal, respectively representing the emission from liquid water and the scattering by dense ice. For Type 3 cases both the emission and the scattering signals increase in a certain ratio while for Type 4 cases the emission signal slows down or stops. The slope in the *D*–PCT scatterplot is then an indication of how fast the dense ice amount grows relative to liquid water. The results of the previous section show that the occurrence of Type 4 pattern and the magnitude of the

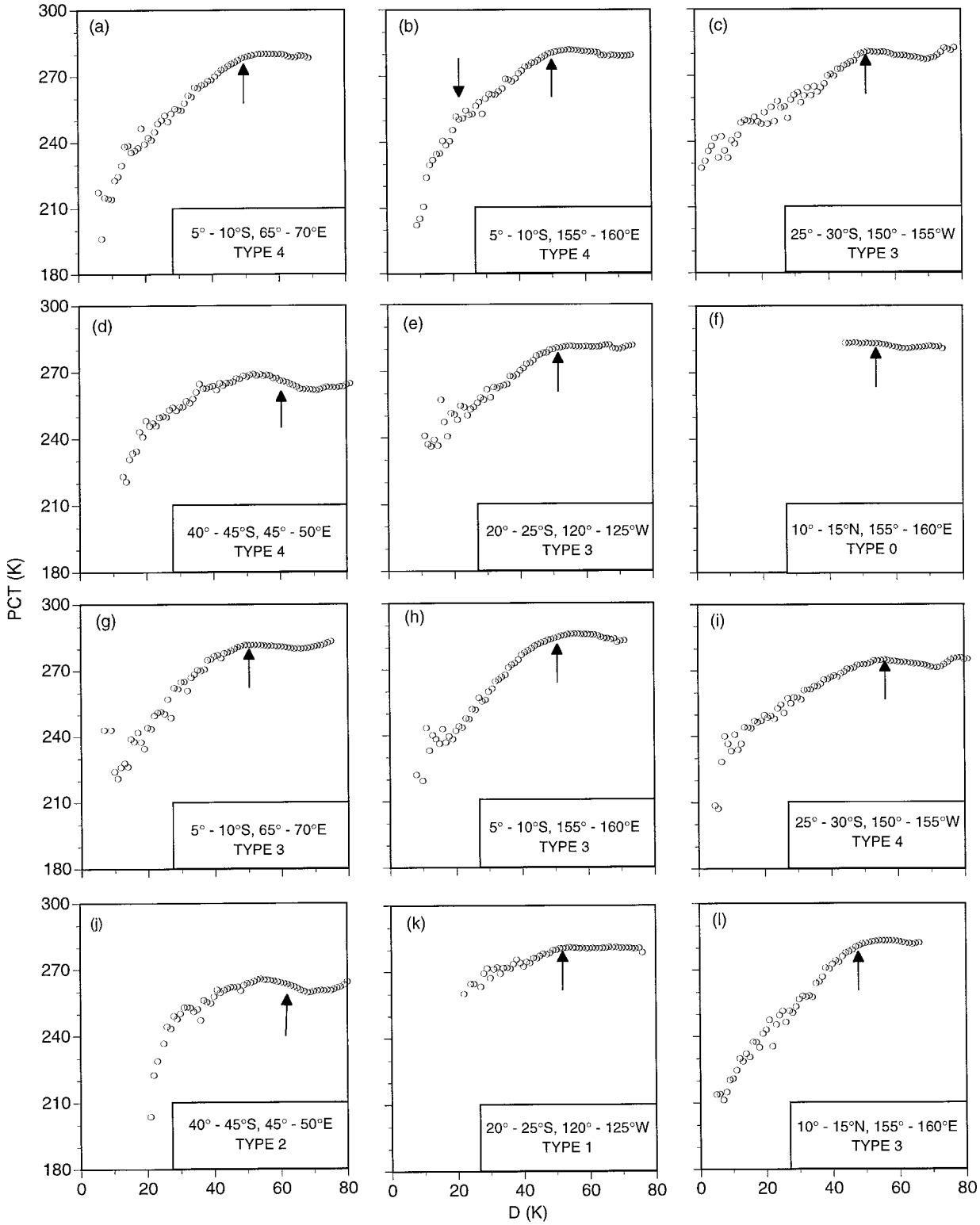

FIG. 10. Monthly and 5° × 5° averaged relationship between D and PCT for the same boxes as those in Fig. 2 while using adjusted α. Up-pointing arrows show the threshold of rainfall.

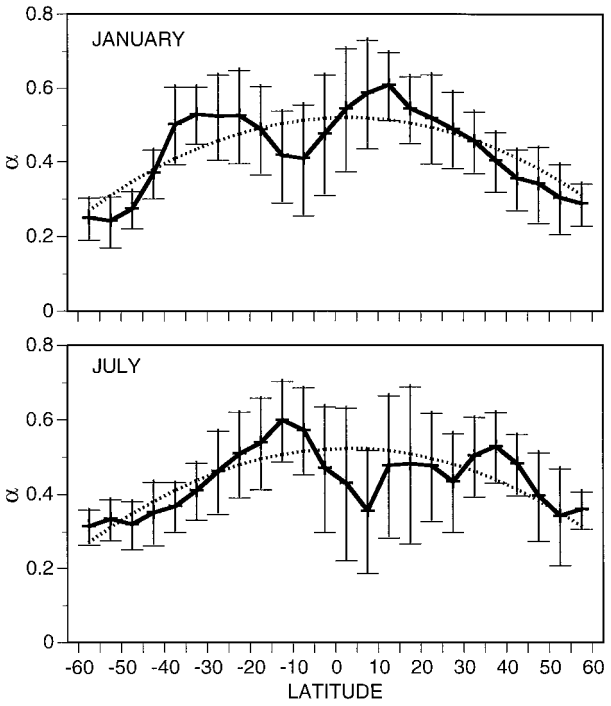

FIG. 11. Latitudinal distribution of adjusted α with standard deviation. The fitting curve of (3) is also shown by dotted curve.

slope do not have a clear latitudinal dependence. Instead, they may occur preferentially in specific regions.

To investigate quantitatively this preference, we have selected nine regions as listed in Table 1, which cover all the regions where Type 3 and 4 *D*–PCT relationships are concentrated. The number ratio of Type 4 to the sum of Types 3 and 4 is shown in Table 2, sorted by the magnitude of the ratio. The three regions with the greatest number ratio are the southwestern Indian Ocean, SPCZ, and the tropical Atlantic Ocean in January and the tropical eastern Pacific Ocean, SPCZ, and the tropical Atlantic Ocean in July. The SPCZ, the tropical Atlantic Ocean, and the tropical eastern Pacific Ocean have larger ratios while the tropical western Pacific Ocean (warm pool), the tropical Indian Ocean, and the south Atlantic Ocean have smaller ratios during both months.

TABLE 1. Selected regions.

Number	Latitude and longitude	Region
1	10°S–10°N, 40°–100°E	Tropical Indian Ocean
2	10°S–10°N, 120°E–180°	Tropical western Pacific Ocean, warm pool
3	10°S–10°N, 80°–130°W	Tropical eastern Pacific Ocean
4	10°–40°N, 120°–160°E	Northwestern Pacific Ocean
5	20°–50°N, 30°–80°W	North Atlantic Ocean
6	10°–40°S, 40°–70°E	Southwestern Indian Ocean
7	20°–40°S, 120°W–180°	South Pacific Ocean, SPCZ
8	20°–50°S, 0°–60°W	South Atlantic Ocean
9	5°S–15°N, 20°–60°W	Tropical Atlantic Ocean

TABLE 2. Number ratio of Type 4 to (Type 3 + Type 4).

Region	Number of Type 3	Number of Type 4	Ratio
January			
Southwestern Indian Ocean	14	18	0.56
South Pacific Ocean, SPCZ	15	14	0.48
Tropical Atlantic Ocean	7	6	0.46
Tropical eastern Pacific Ocean	7	4	0.36
North Atlantic Ocean	21	10	0.32
South Atlantic Ocean	27	12	0.31
Tropical Indian Ocean	23	9	0.28
Tropical western Pacific Ocean, warm pool	31	10	0.24
Northwestern Pacific Ocean	17	0	0.00
July			
Tropical eastern Pacific Ocean	8	8	0.50
South Pacific Ocean, SPCZ	20	18	0.47
Tropical Atlantic Ocean	8	6	0.43
Northwestern Pacific Ocean	26	19	0.42
North Atlantic Ocean	18	10	0.36
Tropical Indian Ocean	23	10	0.30
South Atlantic Ocean	17	7	0.29
Tropical western Pacific Ocean, warm pool	34	5	0.13
Southwestern Indian Ocean	2	0	0.00

Large seasonal changes are seen in the southwestern Indian Ocean and the northwestern Pacific Ocean, which may be caused by the summer monsoon in Africa and Asia. In the North Atlantic Ocean, the ratio remains moderate in both months. In Table 3 the averaged values of slopes in the heavy precipitation regime are shown, sorted by the magnitude of the slope. As expected, the

TABLE 3. Slopes of *D*–PCT relationship in heavy precipitation regime.

Regions	Total number of Type 3 and Type 4 boxes	Slopes
January		
Tropical Atlantic Ocean	13	2.77
Southwestern Indian Ocean	32	2.74
South Pacific Ocean, SPCZ	29	2.30
Tropical eastern Pacific Ocean	11	2.20
North Atlantic Ocean	31	2.18
Tropical western Pacific Ocean, warm pool	41	1.99
Tropical Indian Ocean	32	1.77
South Atlantic Ocean	39	1.69
Northwestern Pacific Ocean	17	0.81
July		
Tropical eastern Pacific Ocean	16	3.24
Tropical Atlantic Ocean	14	2.60
Northwestern Pacific Ocean	45	1.97
Tropical Indian Ocean	33	1.90
South Pacific Ocean, SPCZ	38	1.82
North Atlantic Ocean	28	1.72
Tropical western Pacific Ocean, warm pool	39	1.70
South Atlantic Ocean	24	1.58
Southwestern Indian Ocean	2	0.80

order of regions in Table 3 is similar to that in Table 2, although they are not exactly the same. Of the four tropical regions (numbers 1, 2, 3, and 9 in Table 1) the ratio and the slope is larger in the two regions in the Western Hemisphere (the tropical Atlantic and the tropical eastern Pacific) than those in the Eastern Hemisphere (the tropical Indian and the tropical western Pacific) although the total number of Type 3 and 4 is greater in the later two regions. It is noticed that in the warm pool region, where sea surface temperature remain high (>28°C) throughout the year, the ratio or slope does not show higher values than some of the other regions (as the sea surface temperature does). Instead, they are relatively low. The explanation for this could be that the convection in this region may not be as vigorous so that the amount of dense ice is not as large as those in some of the other regions. Comparisons of in situ measurement are required to verify this interpretation. It should be noted that neither the ratio nor the slope gives information about total precipitation; they indicate only the relative strength of the emission (by liquid water) and the scattering (by dense ice) signals.

An algorithm based solely on the microwave emission signal may work reasonably well for Types 0, 1, and 3. However, it could miss precipitation signals after the emission signal saturates for Types 2 and 4, which accounts for about 15% of the total 5° × 5° boxes examined. This underestimation does not seem to be latitude dependent because there is no clear indication that Types 2 and 4 are more likely to occur in certain latitude(s). On a monthly average basis, the scattering signal PCT is more ideally used for rainfall estimation because it is almost linearly related to the emission signal D in the light precipitation regime and does not saturate in the heavy precipitation regime. However, the strong dependence of PCT on clear-sky and cloud variables in light rain makes it difficult to distinguish no-rain and light rain situations. Combining both the emission and the scattering signals may be the optimal option. Further studies are needed regarding the best possible way to accomplish this combination.

5. PIP-2 cases

PIP-2 is a project that was desired to better understand the strength and weaknesses of current SSM/I precipitation algorithms and to determine specific ways in which to improve them. A total of 28 rainfall cases were chosen for this project that cover a wide range of latitudes and period. Cases from the WetNet PIP-2 are investigated in this section to examine how the different emission–scattering relationships affect the retrievals from emission- and scattering-based algorithms. From the 28 PIP-2 cases, we selected 15 cases that include at least two satellite passes and cover sufficient oceanic area. The D–PCT relationships for the 15 selected cases are shown in Fig. 12, together with the original PIP-2 case numbers and case titles. Similar to the monthly mean diagrams in Fig. 2, the D–PCT relationships show different types and slopes. The three U.K. cases (cases 4, 5, and 6) and the North Atlantic cyclone case (case 18) have the smallest slopes and only a few points with $D < 20$, implying a weak scattering signal. The tropical convective cloud cases of Darwin I and II (cases 12 and 13) and TOGA COARE I (case 27) have the largest slopes implying a strong scattering signal. It is interesting to notice that the hurricane cases (cases 9, 20, 21, and 28) do not have the largest slopes in spite of possibly the strongest convection associated with them. The reason for this result is not clear.

The effects of the difference in the D–PCT relationship on emission- and scattering-based retrievals are studied by examining the performance of two well-established retrieval algorithms: the emission-based algorithm by Wilheit et al. (1977, 1991), and the scattering-based algorithm by Grody (1991) and Ferraro and Marks (1995). Based on radiative transfer model simulations, Wilheit et al. (1991) developed the following relation between rainfall rate (r) and brightness temperatures:

$$T(r) = T_0 + (285 - T_0)[1 - \exp(-r/r_c)] - 3.5r^{1/2}, \quad (4)$$

where $T(r) = 2T_{BV19} - T_{BV22}$, T_{BV22} is vertically polarized brightness temperature at 22 GHz; T_0 is T in the absence of precipitation; and $r_c = 25/F^{1.2}$ where F is the freezing level determined from a comparison of the vertically polarized brightness temperatures at 19 and 22 GHz. The scattering-based algorithm is based on a scattering index (Grody 1991), $\mathrm{SI} = -174.4 + 0.715T_{BV19} + 2.439T_{BV22} - 0.00504T_{BV22}^2 - T_{BV85}$. For $\mathrm{SI} > 10$ the rainfall rate is expressed by (Ferraro and Marks 1995)

$$r = 0.00115 \times \mathrm{SI}^{2.16832}. \quad (5)$$

Both algorithms are applied to all oceanic pixels. A subset of raining pixels with rainfall rate larger than 0.17 mm h^{-1} [$\mathrm{SI} > 10$ translates to $r > 0.17$ according to (5)] by either algorithm is used for the comparison.

The ratio of rainfall rates determined by the emission-based to the scattering-based algorithm ($r_{\mathrm{emission}}/r_{\mathrm{scattering}}$) is also shown for each case by a column diagram in Fig. 12. The comparison is made for total rain (denoted by T in the diagram), light rain ($D \geq 20$, denoted by L), and heavy rain ($D < 20$, denoted by H). For most of the cases, the emission-based retrievals are larger than the scattering-based retrievals (ratio > 1) in the light rain regime while smaller (ratio < 1) in the heavy rain regime. In the five cases (cases 4, 5, 6, 10, and 18) in which the minimum values of D are higher than or around 20, the emission-based retrievals are significantly higher than those of the scattering-based for total rainfall. In several cases (cases 9, 11, 19, 20, and 24) the higher ratio in the light rain regime and the lower ratio in the heavy rain regime cancel to a certain extent, resulting in a smaller bias between the two retrievals in total rain. These cases include frontal systems (cases 11,

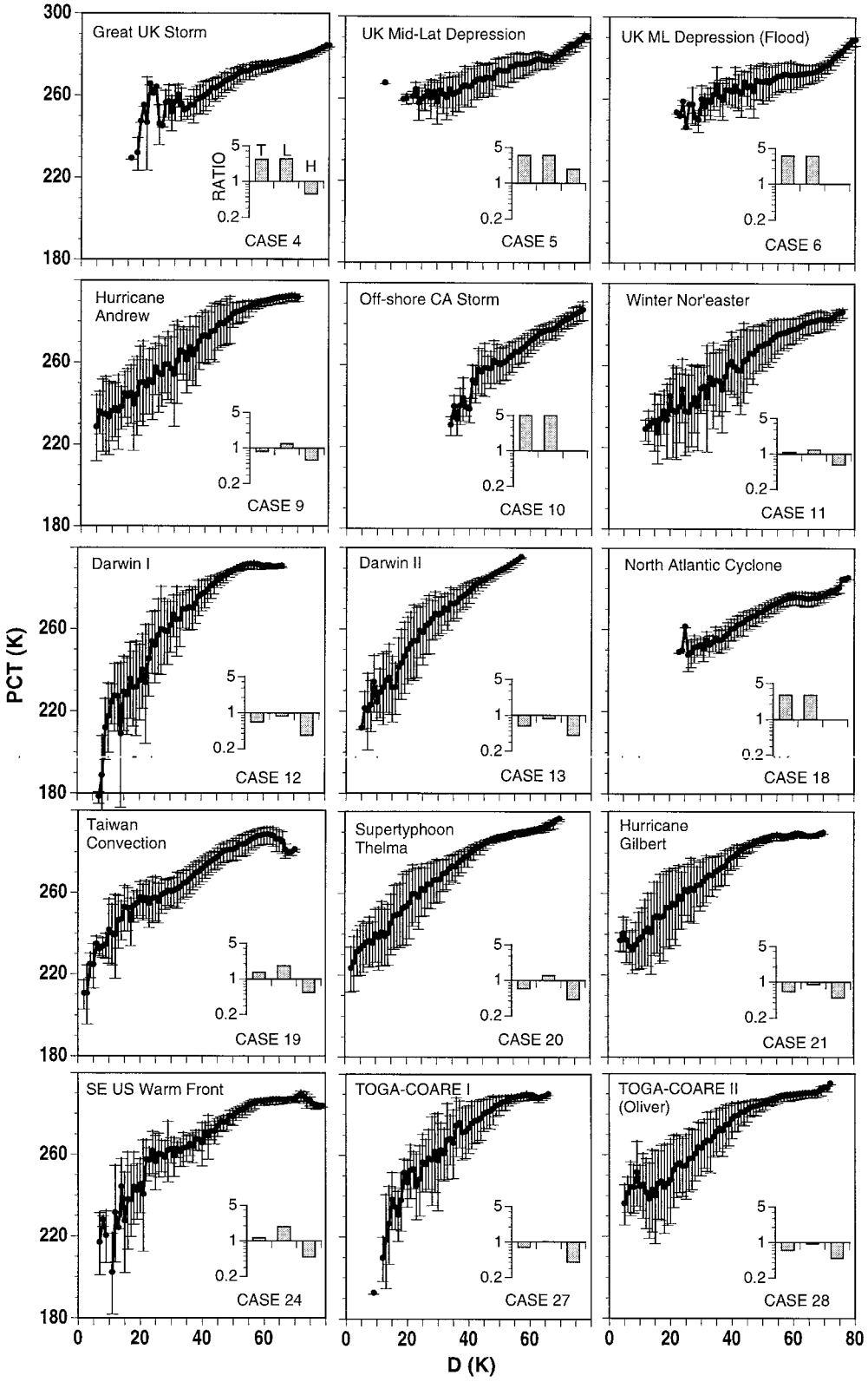

FIG. 12. Relationships between *D* and PCT and ratios of the emission- and the scattering-based retrievals for 15 selected PIP-2 cases. Standard deviation of PCT in each *D* bin is shown by the vertical line. Original PIP-2 case number and case title are also shown. In the ratio diagram, T indicates total rain, L light rain, and H heavy rain.

19, and 24) and hurricanes (cases 9 and 20). In the two Darwin cases that have the largest overall slope in the *D*–PCT plots, the emission-based retrievals are significantly smaller than the scattering-based retrievals for both light and heavy rains though the difference in light rain regime is relatively small. Very small differences are found in the light-rain regime for the two TOGA COARE cases and Hurricane Gilbert case, while the emission-based retrievals are less than half of the scattering-based retrievals in the heavy rain regime.

From these limited cases there seem to be relations between the *D*–PCT pattern and the relative magnitudes of the emission- and the scattering-based retrievals: 1) the emission-based algorithm overestimates rainfall relative to the scattering-based algorithm for Type 1 and some Type 3 and 4 clouds, given their minimum values of *D* being around 20; 2) the scattering-based algorithm overestimates rainfall relative to the emission-based algorithm for the heavy rain regime of Type 3 and 4 clouds; and 3) the ratio of the emission-based to the scattering-based rainfall retrievals is related to the slope in *D*–PCT diagram, steeper slopes corresponding to smaller ratios. Because of the lack of adequate validation data it is impossible to find out which of the two algorithms is more accurate for the entire rainfall spectrum. However, the aforementioned results do indicate that emission- and scattering-based algorithms work favorably in different rainfall regimes; that is, the emission-based algorithm works favorably for the light rain regime while the scattering-based algorithm works favorably for the heavy rain regime. Therefore, both emission and scattering signals are needed to cover the entire rainfall spectrum.

6. Conclusions

The relationship of two parameters observed from microwave satellite data—polarization difference *D* at 19 GHz and polarization corrected temperature PCT at 85 GHz—was investigated over the ocean on a monthly mean basis in order to understand the basic relation of the emission and scattering signals in the natural cloud systems and to provide some guidance to the rainfall algorithm design. Both emission and scattering are influenced by sea surface and clear-sky variables when rainfall rate is low. When the rainfall rate becomes heavy enough, *D* primarily reflects the emission from liquid hydrometeors while PCT mainly reflects the scattering by dense ice above freezing level. These two parameters were averaged in $5^\circ \times 5^\circ$ region for a month. Therefore, the relationship revealed in this study is a large-scale and a long-time mean feature instead of a representation for an individual cloud.

The *D*–PCT slope was studied individually for the nonprecipitation regime, light precipitation regime, and heavy precipitation regime because the dominant factor(s) in determining the slope are different. For the nonprecipitation regime, the fixed coefficient (α) in (2) results in a larger slope in higher latitudes and colder season. By adjusting α, it is possible to minimize the slope in this regime. The change of α value has little effect on the *D*–PCT relationship in the precipitation regimes. In the light precipitation regime, the slope is also latitude and season dependent, but in an opposite way compared to the nonprecipitation regime. The larger slopes are found in the low-latitude warm regions. The explanation for this slope variation is not conclusive. However, it is felt that the difference in dominant cloud types in the lower and higher latitudes contributes the most to this slope difference. Lower-latitude clouds are more convective, which leads to growth in both horizontal and vertical dimensions as rainfall rate increases, resulting in larger slopes. The slope in the heavy precipitation regime provides a relative measure of the dense ice amount compared to the liquid water amount. It may also be an indicator of the vigor of the convection because only strong convection can produce a large amount of dense ice. No clear indication was found in the heavy precipitation regime that the slopes are latitude dependent. Rather, the large slope values are usually observed in some particular regions, such as the tropical Atlantic, SPCZ, and the tropical eastern Pacific. The southwestern Indian Ocean in January and the northwestern Pacific Ocean in July also have large slopes. Again, the warm pool and the south Atlantic are among those regions having smaller slopes.

A study of the relative performance of an emission-based algorithm and a scattering-based algorithm was done using WetNet PIP-2 cases. The results show that the ratio of retrievals from the two different algorithms is very different in the light rain regime from the heavy rain regime, indicating the differences between the algorithms. The *D*–PCT slope also has clear relation to this ratio. The implication of the *D*–PCT relationship revealed in this study for rainfall retrievals arises from the following two aspects. First, the results emphasize the necessity of incorporating the scattering signal in rainfall rate retrieval algorithms, although it is usually considered that the emission signal is more directly related to rainfall over ocean. Second, the *D*–PCT slope information could help categorize precipitation types, which may be useful in applying a proper algorithm to a certain precipitation type. Coupling the emission and the scattering signals in rainfall algorithms is expected to be optimal in obtaining better rainfall estimates. The precipitation type obtained from the *D*–PCT slope could provide some guidance for the optimal method with which to accomplish this coupling.

Acknowledgments. Comments from three anonymous reviewers were very helpful. This research was supported by NASA NAGW-3997 and NASA NAGW-1960. SSM/I data were provided by NASA Marshall Space Flight Center Distributed Active Archive Center.

REFERENCES

Adler, R. F., A. J. Negri, P. R. Keehn, and I. M. Hakkarinen, 1993: Estimation of monthly rainfall over Japan and surrounding waters from a combination of low-orbit microwave and geosynchronous IR data. *J. Appl. Meteor.,* **32,** 335–356.

Devlin, K. I., and E. J. Zipser, 1996: Mesoscale convective systems defined by their 85-GHz ice scattering signature: Size and intensity comparison over tropical oceans and continents. *Mon. Wea. Rev.,* **124,** 2417–2437.

Ferraro, R. R., and G. F. Marks, 1995: The development of SSM/I rain rate retrieval algorithms using ground-based radar measurements. *J. Atmos. Oceanic Technol.,* **12,** 755–770.

Greenwald, T. J., G. L. Stephens, T. H. Vonder Haar, and D. L. Jackson, 1993: A physically based retrieval of cloud liquid water from SSM/I measurements. *J. Geophys. Res.,* **98,** 18 471–18 488.

Grody, N. C., 1991: Classification of snow cover and precipitation using the Special Sensor Microwave/Imager (SSM/I). *J. Geophys. Res.,* **96,** 7423–7435.

Heymsfield, G. M., and R. Fulton, 1994: Passive microwave and infrared structure of mesoscale convective systems. *Meteor. Atmos. Phys.,* **54,** 123–139.

Liu, G., and J. A. Curry, 1992: Retrieval of precipitation from satellite microwave measurement using both emission and scattering. *J. Geophys. Res.,* **97,** 9959–9974.

——, and ——, 1993: Determination of characteristics features of cloud liquid water from satellite microwave measurements. *J. Geophys. Res.,* **98,** 5069–5092.

——, ——, and M. Weadon, 1994: Atmospheric water balance in Typhoon Nina as determined from SSM/I satellite. *Meteor. Atmos. Phys.,* **54,** 141–156.

——, ——, and R.-S. Sheu, 1995: Classification of clouds over the western equatorial Pacific Ocean using combined infrared and microwave satellite data. *J. Geophys. Res.,* **100,** 13 811–13 826.

Petty, G. W., 1990: On the response of the Special Sensor Microwave/Imager to the marine environment—Implications for atmospheric parameter retrievals. Ph.D. dissertation, University of Washington, 291 pp. [Available from Dept. of Atmospheric Sciences, University of Washington, Seattle, WA 98195.]

——, 1994a: Physical retrievals of over-ocean rain rate from multichannel microwave imagery. Part I: Theoretical characteristics of normalized polarization and scattering indices. *Meteor. Atmos. Phys.,* **54,** 79–99.

——, 1994b: Physical retrievals of over-ocean rain rate from multichannel microwave imagery. Part II: Algorithm implementation. *Meteor. Atmos. Phys.,* **54,** 101–121.

——, 1995: Frequencies and characteristics of global oceanic precipitation from shipboard present-weather reports. *Bull. Amer. Meteor. Soc.,* **76,** 1593–1616.

Smith, E. A., A. Mugnai, H. J. Cooper, G. J. Tripoli, and X. Xiang, 1992: Foundations for statistical–physical precipitation retrieval from passive microwave satellite measurements. Part I: Brightness-temperature properties of a time-dependent cloud-radiation model. *J. Appl. Meteor.,* **31,** 506–531.

Spencer, R. W., H. M. Goodman, and R. E. Hood, 1989: Precipitation retrieval over land and ocean with SSM/I: Identification and characteristics of the scattering signals. *J. Atmos. Oceanic Technol.,* **6,** 254–273.

Wilheit, T. T., A. T. C. Chang, M. S. V. Rao, E. B. Rodgers, and J. S. Theon, 1977: A satellite technique for quantitatively mapping rainfall rates over oceans. *J. Appl. Meteor.,* **16,** 551–560.

——, ——, and L. S. Chiu, 1991: Retrieval of monthly rainfall indices from microwave radiometric measurements using probability distribution functions. *J. Atmos. Oceanic Technol.,* **8,** 118–136.

——, and Coauthors, 1994: Algorithms for the retrieval of rainfall from passive microwave measurements. *Remote Sens. Rev.,* **11,** 163–194.